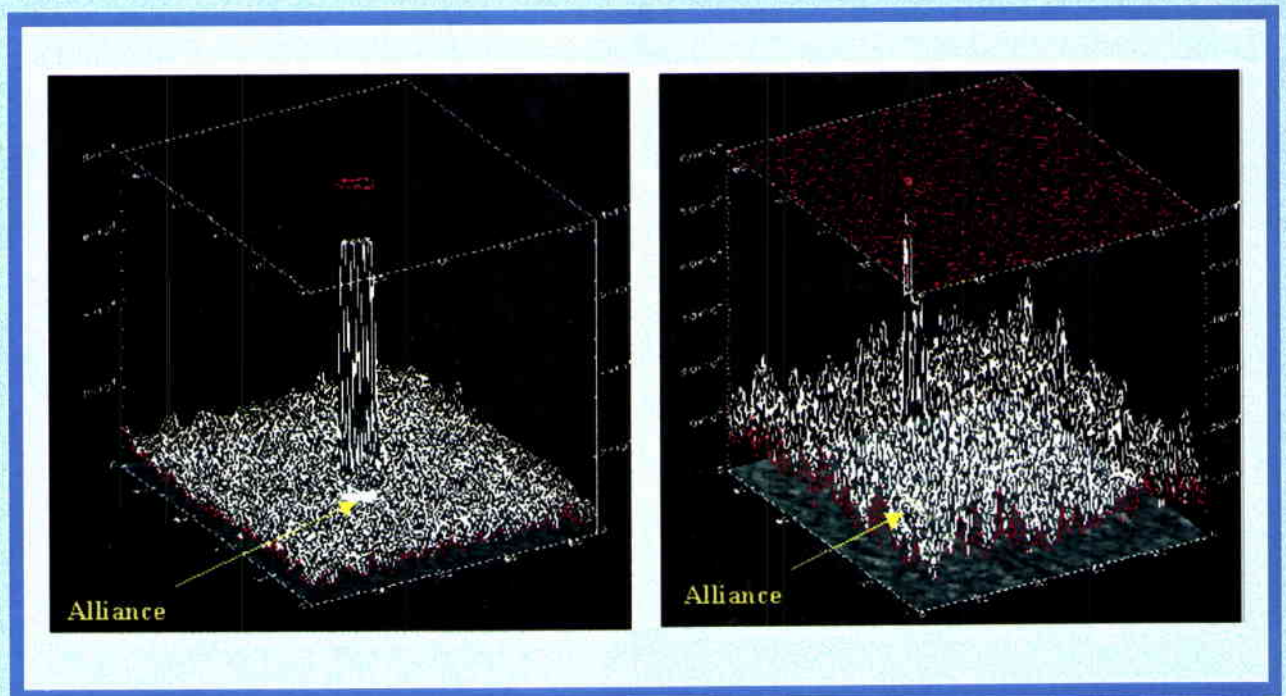# SACLANT UNDERSEA RESEARCH CENTRE REPORT

An automatic approach to ship detection in spaceborne synthetic aperture radar imagery: an assessment of ship detection capability using RADARSAT

Farid Askari, Benoit Zerr

December 2000

NORTH ATLANTIC TREATY ORGANIZATION   ORGANISATION DU TRAITE DE L'ATLANTIQUE NORD

SACLANTCEN SR-338

An Automatic Approach to Ship Detection in Spaceborne Synthetic Aperture Radar Imagery: an Assessment of ship detection capability using RADARSAT

Farid Askari, Benoit Zerrr

Jan L. Spoelstra
Director

intentionally blank page

SACLANTCEN SR-338

An Automatic Approach to Ship Detection in Spaceborne Synthetic Aperture Radar Imagery: an Assessment of ship detection capability using RADARSAT

Farid Askari, Benoit Zerr

Executive Summary: Precise rapid reconnaissance of shipping in the littoral region is vital to shipboard self-defense systems, ASW, mine-hunting and clearing systems. The goals of this investigation are to develop an automated procedure for ship and wake detection in space-based synthetic aperture radar (SAR) imagery, and to assess the capabilities of the various RADARSAT SAR imaging modes.

Although ship identification and classification are beyond the capabilities of existing commercial sensors, localization and extraction of ship size, and heading are feasible. The generic nature of the algorithms described here implies applicability beyond SAR ship detection. The methods can be incorporated in to ship or AUV-based systems that deal with pattern recognition and target detection. Further work includes more effective coupling of the different approaches.

intentionally blank page

SACLANTCEN SR-338

An Automatic Approach to Ship Detection in Spaceborne Synthetic Aperture Radar Imagery: an Assessment of ship detection capability using RADARSAT

Farid Askari and Benoit Zerr

Abstract: This report describes a methodology for automated ship and wake detection in space-based synthetic aperture radar (SAR) imagery. The methodology incorporates a multistage approach involving several algorithms which can be applied according to requirements, computational resources, and scene composition. We suggest that the localized K-distribution be used for scene segmentation and identification of regions containing probable targets. For a more detailed quantitative scene analysis and accountability for probabilities of occurrence of targets in conjunction with other oceanic features, a coupled neural-networks/Dempster-Shafer detection system is used. The mathematical morphology algorithm is better suited for SAR imagery with low signal-to-clutter ratios, as it incorporates neighbouring information and signal amplitudes for target detection. The methods are tested on several RADARSAT images with different imaging geometry and beam modes. On the basis of our findings, concerning the use of different RADARSAT imaging modes, we demonstrate conclusively that the STANDARD beam is far superior to SCANSAR-NARROW beam for automatic ship detection

Keywords: remote sensing, ship detection, K-distribution, artificial neural networks, RADARSAT, Hough transform.

Contents

SACLANTCEN SR-338

1
Introduction

The utility of space-based synthetic aperture radar (SAR) as a surveillance tool has been recognized for over twenty years due to its all-weather/day-night imaging capabilities. Many nations rely on spaceborne SAR for monitoring of their territorial waters, specifically: fisheries management, and pollution. Precise and rapid reconnaissance of shipping traffic/density in the littoral region is equally vital to ship self-defense systems, ASW, and mine-hunting/clearing systems.

Detection of a ship by SAR depends on its size, shape, structure, and orientation to the radar, as well as the background sea clutter. There is an abundance of ship/wake detection algorithms in the literature [1- 4]. But these studies mostly cite image processing algorithms for detecting hard target returns or linear features associated with wake signatures. Many of the algorithms are inadequate when the SAR image contains ships in conjunction with complex features such as oceanic fronts, eddies, swells and internal waves. Preliminary investigations suggest that a knowledge-based automated scene description system approach may be appropriate. A neural-network-based automated ocean-feature-detection system [5] to facilitate detection of hard targets is described and compared with other pattern recognition algorithms. The original image can be represented as a series of features, with every feature having a corresponding probability of occurrence, as well as certainty or belief factors explained by evidential reasoning theory [6]. Another novelty of the present work is the availability of sea-truth and aircraft surveys, often unavailable in purely theoretical studies.

In Section 2, we discuss the methodologies for ship hard target and wake detection in SAR imagery. The results of applications of the techniques and discussions are given in Section 3. Conclusions are given in Section 4.

2

Methods

Detection of ships and wakes is essentially a pattern recognition problem. Speckle noise and false targets resulting from natural surface features complicate the detection problem. The principal factor limiting ship/target detectability in SAR imagery is the sea-clutter. The sea-clutter or mean radar back-scattering cross-section from the ocean is a function of radar frequency, polarization, wind speed, incident angle, azimuth angle and resolution cell. Clutter is the collection of return echoes from scatterers within the resolution cell of the antenna. Fluctuations occur because of motion and changes in the amplitude and phase of the scatterers during the imaging process. Hence, for estimating the radar performance it is essential not only to quantify the mean backscattering signal, but also to characterize the statistical characteristics of the signal. We discuss the influence of the mean radar cross-section on ship detectability, then examine radar fluctuation statistics in the context of probability density functions (PDF). For automatic hard target detection, two techniques are presented: the Neural-Network-Dempster-Shafer hereinafter referred to as NNDS, and a mathematical morphology (MM) algorithm. The NNDS technique relies on the amplitude of the signal-to-clutter ratio using a Gaussian-shaped kernel. MM uses neighboring pixel information for 2-D shape detection. We end the section with a method for wake detection using the modified Hough transform which was initially developed and tested on ERS-2 SAR imagery.

2.1 Influence of sea clutter on ship detection

Only a limited amount of information exists in the unclassified literature [3] on the relationship between a ship's size and type, and its radar cross-section:

$$L = \left(\frac{\sigma_{ship}}{0.08 R(\theta)} \right)^{3/7} \quad , \quad R(\theta) = 0.78 + 0.11\theta \tag{1}$$

where σ_{ship} is the radar cross-section of the ship in square meters, L is the ship length and θ is incidence angle. The minimum detectable ship-radar-cross-section can be written as

$$\sigma_{ship}^{min} = \rho_r \rho_a 10^{(\sigma_0 + T)/10} \tag{2}$$

where ρ_r and ρ_a are respectively the range and azimuth resolutions of the radar, σ_0 is the background sea clutter (normalized radar cross-section for either VV or HH polarization), and T is a threshold above the mean background.

The most widely used model for describing the mean background clutter at C-band has been the CMOD4 algorithm [7]. This algorithm has been extensively applied and tested using the SAR and scatterometer data from the ERS-1/2 satellites that operate in the vertically polarized transmit/receive (VV) configuration. For RADARSAT SAR, however, because of its horizontally polarized transmit/receive (HH) configuration, a modified version of CMOD4 algorithm has been suggested [8]:

$$\sigma_0^H = \frac{\left(1 + \alpha \tan^2 \theta\right)^2}{\left(1 + 2 \tan^2 \theta\right)^2} \sigma_0^V (U, \theta, \phi) \qquad (3)$$

In equation 3, U, θ, ϕ are respectively, the wind speed, incidence angle, and azimuth angle of the radar with respect to the wind direction, and σ_0^H and σ_0^V are the HH and VV radar cross-sections, and α is a parameter that has been empirically estimated [8].

With the aid of Equation (3) in (2) and using nominal values for the range and azimuth resolution, we arrive at vessel sizes that are detectable (Table 1) in RADARSAT imagery under varying wind speeds, incidence angles and azimuth angles. The plot of background clutter at C-band (Fig. 1) reveals several qualitative observations: 1) for a constant wind speed and incidence angle, ship detection performance improves (because of the lower clutter) if the radar is perpendicular to the wind direction (cross-wind) *versus* parallel to the wind (upwind/downwind) direction; 2) at a fixed incidence angle, ship detection performance degrades (because of the increase of the clutter) with increasing wind speed; 3) for a fixed wind speed, ship detection performance is enhanced when the ships are positioned within the far-range (steeper incidence angles) *versus* the near-range (shallow incidence angles) of the image swath.

2.2 Clutter statistics

The easiest way to search for targets in an image is to examine the intensity of each pixel and decide whether or not it belongs to a target. However, for reliable detection the statistical properties of the pixel intensity of the clutter and the target must be known. The radar clutter distribution from the ocean is frequently described by a Rayleigh distribution [3]. However, Non-Rayleigh statistics can occur with the addition of small number of large scatterers such as sea spikes or deletion of a large number of small scatterers (shadowing mechanism) from the resolution cell. Increases in the spatial resolution of the radar can also contribute to non-Rayleigh statistics. When high reflectivity scatterers such as sea spikes or targets appear within the radar resolution cell, the distribution tail is elongated. To fit such long-tailed clutter data, the Weibull or the K distributions have been used [3,9], as they are mathematically tractable. The "K-

distribution" is specified by the mean and normalized variance. The former shows the average signal strength, the latter deviations from an exponential distribution.

2.3 Hard target detection

The hard target radar return from a ship is governed by several mechanisms including: direct reflection from areas perpendicular to the radar beam, corner reflections and scattering from ship, and multiple reflection from the ship and the sea surface [10]. Other parameters also affect the radar return such as material make-up of the ship, the 3-D infrastructure, incidence and aspect angles, and radar frequency and polarization. Motion effects (speed, roll, heave) will also reduce the coherence of radar signal backscattered from a ship, resulting in smearing and reduction in peak pixel intensity. Studies involving ship detection using multiple frequencies showed enhancements for shorter wavelength (higher frequency) SARs. Azimuthal ship track orientation relative to satellite ground track yields superior results [10].

Automatic hard target detection involves extracting bright point-like targets (relative to the background) from the SAR image plane. With SAR spatial resolution of 25 m, ship signatures often appear blob-like rather than point-like targets. A standard indicator of ship structure is the length-to-width ratio (L/W)[10]. Merchant ships have L/W of the order of 6-7, whereas military vessels (destroyers, carriers) have L/W greater than 10. For point/blob-like target detection we use idealized Gaussian-shaped 1-D profiles. As described in [5] a 2-D image is first processed by sub-dividing it into series of sub-blocks. Four separate 1-D profiles with different orientations are extracted from each sub-block and the results are processed through a bank of neural networks (Fig. 2). For each 1-D profile, the network produces an independent decision and belief that the detected profile belongs to a predefined shape, in this case a Gaussian-shaped profile (Fig. 3). The individual opinions are fused using the DS rules to derive the final classification.

The neural network architecture used relies on radial basis functions (RBF) for training and pattern classification [5]. The neural network consists of three layers: input nodes, basis function (BF) nodes, and the output nodes. The connections between the input nodes and second layers have unit weights. The second layer is made of a number of multi-dimensional Gaussian BF defined by a mean vector and covariance matrix. The mean vectors are computed from the training set by a fuzzy c-means clustering algorithm [11], where the number of clusters is equal to the number of BF needed by the network. The network output nodes are activated using a linear combination of the BF node the weights of which is determined using a matrix pseudo-inverse approach. The RBF classifier is essentially a function mapping interpolation method that partitions the n-dimensional measurement space into hyper-volumes or regions belonging to the separate classes. The outputs of the RBF for each 1-D profile are fused by the Dempster-Shafer (DS) process for obtaining final probabilities of occurrences of hard targets. The DS method developed in [5] for ocean feature detection is modified to recognize hard targets. As a hard target signature can be approximated by a nearly isotropic profile, the DS-combination-rule [5] can be forced to look for a Gaussian-shape on every 1-D profile.

The NNDS technique described above relies on signal-to-clutter-ratios or grey-level information which extends over a wide dynamic range. The two other approaches considered (the statistical K-distribution and the MM algorithm) operate on binary or thresholded images. The 2-D MM algorithm method involves a two-stage process. First, the image is transformed into a binary image by setting all pixel values below 255 level to zero. The second stage involves convolving the image with the erosion algorithm. The performance of this algorithm is contingent on choosing an optimum kernel size that depends on the spatial coherence of the data. The erosion operation in morphological processing is described in [12]. The last step in the analysis is the pixel connection process, which is also known as connected component analysis. Here we use four adjacent pixels to merge the connected pixels into a single cluster.

2.5 Wake detection

According to the hydrodynamic Kelvin wave theory [13] developed in 1887 several wave patterns result from the motion of a ship in the water: the Kelvin or bow wave envelope, the cusp waves which form the Kelvin envelope, the stern waves, the turbulent wave, and internal waves. Depending on the spatial resolution, radar frequency, wake orientation with respect to the antenna look direction and the background sea-clutter, some or all of these wake structures can be delineated in spaceborne SAR imagery. Often the most visible signature is the turbulence-induced dark streak that can trail the ship for several km. The other dominant signature is the "V"-shaped pattern, which can have opening angles varying between 6° and 52". Radar imaging theories explaining the formation of narrow angle "V"-shaped patterns have been developed in [14-16]. A detailed simulation study of radar imaging of Kelvin arms of ship wakes is given in [17]. Simulations show that signatures of Kelvin arms are strongest at low wind speeds and are not particularly sensitive to wind direction. The signatures, however, are much sensitive to radar look direction and wake orientation. Furthermore, the signatures are more clearly visible on L-band than on C-band SAR imagery [17].

Several methods for line detection in SAR images have been reported in the literature [18-19]. The Radon transform works in the Fourier domain, while Hough transform (HT) works in the original image plane. On the basis of working with ERS-2 SAR imagery we developed a procedure which relies on the HT for automatic detection of wakes in SAR imagery (Fig. 4). Straight-line HTs are classified in terms of parameters used to formulate the Hough space. The most popular parameterization is given by

$$\rho = x\cos\theta + y\sin\theta \qquad (4)$$

ρ is the distance from the line to the origin
  and,
θ is the angle between the line and the abscissa

Equation (4) maps a point in the image space into a curve in the Hough space. After the HT is performed, the Hough space is searched for a number of maxima points, each of

– 6 –

which corresponds to a straight line in the image space. Here the HT is modified to deal with line segments. The HT is run to determine the equation for a line from the maxima in the Hough space, then for extracting the starting and ending points of the line segment. Line segments are not directly sought, as the HT would become computationally inefficient.

SACLANTCEN SR-338

3

Results and Discussions

3.1 RADARSAT imagery

In this section we analyze the RADARSAT images collected during SACLANTCEN's MAPEX-2000 and Boundary-2000 experiments. The SAR images were acquired over the southeastern coast of Sicily near the Malta Plateau between 21 February and 16 March, and 29 April to 4 May 2000 during two separate cruises. Two types of images were acquired for assessing the ship detection capabilities of the various beam modes (Fig. 5): SCANSAR and STANDARD [18]. The first four images were collected in the SCANSAR – Narrow imaging mode (Table 2). In this mode, between two (SNA:W1+W2) to three (SNB:W2+S5+S6) single beams are employed during data collection, providing maximum spatial coverage (300 km). The beams are selected sequentially, thereby creating a wider swath than is possible from a single beam. The increased swath coverage, however, comes at the expense of reduced spatial resolution over a single beam. The nominal range and azimuth resolutions are 50x50 m respectively. The incidence angles for March 3,10, and 12 cover the range of 31 to 46^0, and 20 to 39^0 for March 2.

The last three images were acquired in the STANDARD beam mode. In this mode there are seven beam positions labeled S1- S7. Each beam covers a minimum ground swath of 100 km. The azimuth resolution is the same for all beam positions, 27 m, whereas the range resolution (25 m nominally) changes from beam to beam. The principal advantage of STANDARD beam over the SCANSAR mode is its radiometric image quality, where pixels are represented as 16-bit gray levels. The STANDARD beam mode also offers more flexibility in the choice of incidence angles. The final images are re-sampled to 25 m per pixel in both directions for SCANSAR mode, with intensity values ranging between 0 to 255 digital counts (8-bit), and 12.5 m for STANDARD mode with intensity values ranging between 0 to 65536 digital counts (16-bit).

Figures 6-12 show RADARSAT images for the March and April-May experiments. The March 2 and 3 images were acquired under high-wind and high sea-state conditions, while for March 10 and 12 conditions were moderate. The conditions for the April-May experiment were high to moderate (Table 3)

3.2 Detection results

As a pattern recognition system the human eye is superior to any numerical scheme for detecting objects in satellite imagery. The major obstacles for visual detection, however, are excessively high data volumes and time involved in image interpretation. As a typical RADARSAT image covers an area of 96000 km^2 and consists of 11000x14000 pixels, automatic detection offers clear advantages. Nevertheless some situations call for verification that can only be delivered through visual inspection. In fact, in support of the satellite-ship detection and validation experiments, three MPA flights were conducted out of Sigonella, Sicily during March 2, 3, and 10 with the aim of providing ground-truth information namely: ship positions, speeds, lengths, and headings in the operating area during the satellite overpasses. The MPA surveys, however, did not provide fruitful results and we resorted to visual inspection of SAR imagery for verification of satellite results. As an example the March 10 (Fig. 8) scene is shown where the spatial correlation between the MPA-observed ship positions *versus* the SAR-derived ship positions is less than 25 percent. We attribute the poor agreement to several factors. First, the ship positions (reported by the aircraft's inertial navigation system (INS)) were recorded only to the nearest minute of latitude/longitude. This round-off factor alone can contribute to localization errors of about 1.8 km (equivalent to 30-40 SAR-pixels). Second, the ship speed and heading estimates were somewhat subjective. The MPA navigator used visual clues for judging the parameters. Also, given that there was as much as three hours time-delay between the MPA-survey and satellite overpass (three-hours for March 10), misjudging the ship speed for example by one-knot, could accrue a 4.8km localization error. Hence, we use the results of the visual detection for ground-truth and quantifying the performance of the various algorithms.

The back-scattered signal from the *R/V Alliance* provides an opportunity for extracting ship size and ship heading from SAR imagery in the highly varying ocean environment. Out of the seven SAR images examined the *R/V Alliance* was visible in five scenes. The March 2 and 12 images were not considered for analysis, because in the first case the ship's hard-target return was below the background clutter, and in the second, the ship was docked in port during the satellite overpass. For March 2, the ocean back-scattering strength appears to be stronger than back-scattering from land. The most probable cause of this was perhaps the improper setting of the automatic gain control (AGC) on the receiver. Problems with the AGC are not uncommon with RADARSAT and have been reported elsewhere. The *R/V Alliance* hard target signal-to-clutter-ratio varies from 2.6 to 10.8 dB as a function of background environment as seen graphically (Fig. 13). For March 2, with wind speeds of 11 m/s and 4 m wave heights, the hard target return is submerged below the ocean clutter. The highest signal-to-clutter-ratio is associated with May 4 which has the lowest wind and sea state conditions. Except for March 10, and May 4 images the back-scattering returns from the ship do not exhibit any particular structure and appear as white blobs in the imagery. For May 4 the ship return has more backscatter in the front and back than in the middle. The *Alliance* vessel length is estimated from the number of bright pixels from March 3, 10, April 29, 30 and May 4 to be respectively, 246, 127, 125, 137 and 125 m. The dimensions of the *Alliance* are 92 m in length and 15.2 m in width. Furthermore, we can estimate ship heading (with 180° ambiguity) using the largest dimension of the hard-target-return (length) if the ship has no visible wake signature. For 3 March and 4 May, the SAR-derived headings are respectively, 298° and 76° as compared to 292° and 81° *in situ*-measured headings.

SACLANTCEN SR-338

An inherent problem that arises in matching navigation data from satellite and ship records is localization error. With satellite ground speeds of 7 km/s, small differences in clock-settings on either platform can contribute to sizable localization errors. In this case the localization errors between the INS-derived ship positions *versus* SAR-derived ship positions vary from (Table 2) about one to five ship lengths (90 to 428 m).

We now compare PDF's and higher moment statistics obtained from different sub-regions. The results reveal several notable characteristics (Fig. 14). Regions containing low scatterers in SCANSAR (8-bit) imagery show typical Rayleigh-distribution (Fig. 14a-b). For regions containing high-intensity scatterers, however, the distributions are atypical. Here the distributions are long-tailed, but are somewhat skewed toward the low-intensity values. Also the distributions are peaked at the highest value (255 level) suggesting that the data was clipped during post processing. This operation essentially groups all intensity values associated with ships and sea spikes that are equal to or greater than 255 into the same intensity bin.

For the STANDARD beam (16-bit) imagery, clutter regions containing high-intensity scatterers are characterized by right-skewed-long-tailed distributions that are well suited to the K-distribution (Fig. 14c-d). Moreover, whenever a ship appears within a sub-region, the tail of the distribution becomes longer. As such with a fitted PDF at hand, it is possible to determine if a particular intensity value is due to a target, by comparing the intensity value to a critical intensity which can be set *a priori* by choosing an acceptable false alarm rate. The problem associated with a statistical target detector, however, is one of choosing the appropriate window size for detection. The window must be large enough to produce sufficient statistics, while it must be small enough for target localization. Using several iterations (and a false alarm rate of 5 percent) we arrive at a window size of 20 x 20 pixels for identifying the most probable sub-regions containing hard targets.

Next we apply the NNDS algorithm to a sub-region of a SCANSAR image containing the *R/V Alliance*. In this case the classifier generates an unacceptably high number of false targets (Fig. 15a). As the NNDS algorithm operates on a range of gray scale intensities instead of a set threshold image, the high false alarm rate is attributed to the artificial clipping of high intensity values, or improper selection of the most significant data bits. Given that the hard target signatures only occupy the highest intensity levels (255), a binary image is therefore a more ideal representation for the SCANSAR data. As seen in Figure (15b), applying the MM algorithm to the same sub-region improves detection performance significantly and reduces the false alarm rates. Through the use of neighbouring information, the MM algorithm is able to eliminate many of the "salt-pepper" patterns in the imagery that is often associated with individual sea spikes or speckle noise.

We now show the results of the application of the NNDS algorithm to the STANDARD imagery (Fig. 10-12). Because of the data's high radiometric fidelity (16-bit), the hard target signatures appear at least 5 dB above the background clutter in this type of imagery. Among the April 29, 30 and May 4, the lowest signal-to-clutter ratio is associated with April 30, when the SAR imaging geometry is such that the spacecraft antenna is pointing into the wind (upwind), hence observing a higher contribution from the background clutter. The NNDS detection performance exceeds 97 percent accuracy

for all three STANDARD scenes. The basis for quantifying the performance is through comparisons with visual observations.

The *R/V Alliance's* wake signature was only visible on April 30. During the overpass the ship was moving south at a speed of 12.6 knots. Using wake orientation as the basis for heading, the SAR-derived and *in situ*-measured headings are nearly identical. Figure 16 shows the results of wake detection using the modified HT procedure. Here, the procedure outlined in the previous section was applied twice to the original image (Fig. 16a). The red line corresponds to center-line turbulent wake, and the green line corresponds to a single arm of the Kelvin wake (Fig. 16b). Because the ship is travelling almost parallel (180°) to the satellite flight track, we see no evidence for the "Doppler offset" or ship displacement from its wake signature. The "Doppler offset" is a well-known phenomenon which results from line-of-sight component of motion of scatterers during the aperture formation. However, because it is a cosine-dependent function, the maximum offset is observed for range-travelling targets. In our case the ship velocity cannot be extracted because the ship is moving in the azimuth direction.

SACLANTCEN SR-338

4

Conclusions

In this report we examined three approaches for ship detection: the combined NNDS architecture, a statistical approach utilizing the K-distribution, and mathematical morphology (MM). The three approaches differ in terms of complexity and computational efficiency. The first approach relies on signal-to-clutter-ratios or gray-scale which extends over 16-bit range of values, whereas the other two operate on binary or threshold images. We can draw several general conclusions from the work presented here:

1. The isotropic Gaussian-shaped kernel used in training the NN is well suited for detecting hard target radar returns from ships in SAR imagery.

2. The MM algorithm, which is conceptually simple and computationally efficient, outperforms the NNDS algorithm in detecting hard targets in imagery which has been artificially clipped or thresholded.

3. Of the three approaches considered here, the NNDS is the most computationally intensive. The training of the neural network is rather simple and straightforward, requiring little computation overhead. However, the computation overhead is in the Dempster-Shafer stage where different hypotheses must be tested.

4. On the basis of comparisons with visual interpretations the NNDS shows over 97% success rate in ship detection.

5. The recommended approach for ship detection is scene-segmentation using the k-distribution for identifying regions having the highest probabilities for finding targets, followed by application of NNDS for more precise localization.

The RADARSAT images were collected under a wide range of environmental conditions. The observations from this study have provided the following insights on the use of the two imaging modes for operational ship detection:

1. While ships can be detected visually in SCANSAR imagery, in spite of its extended swath width (300 km), it is not the recommended mode for automatic ship detection due to the poor radiometric resolution.

2. The 8-bit quantization scale provides insufficient dynamic range for discriminating between bright targets and sea clutter under high sea-state and high wind conditions. Because of problems with signal saturation and distorted statistics, application of automatic detection algorithms to SCANSAR imagery produce unacceptably high false alarm rates.

– 12 –

3. When using the SCANSAR imaging mode, the SNB is the preferred choice over SNA because of the coverage of the higher incidence angles where background clutter tends to be lower.

4. The STANDARD beam S6 is perhaps the optimum imaging mode because of its high spatial-radiometric resolution and lower clutter levels at the higher incidence angles.

5. Because of low signal-to-clutter ratios RADARSAT imagery does not appear to be well suited for wake detection.

6. Using wake orientation as a basis for estimating ship heading, SAR-derived headings are nearly identical to *in situ* measured headings. In the absence of a visible wake, it is still possible to assign a ship heading (with 180 ambiguity) based on the orientation of the ships largest dimension. This method yields headings that are within 5° of the *in situ* measured headings.

7. On the basis of hard target response obtained from the *R/V Alliance*, the ship-size tends to be overestimated by at least a factor of 2 and 1.4 respectively, using SCANSAR and STANDARD imagery. More observations are needed, however, because of the sensitivity of this parameter to azimuth viewing angle.

SACLANTCEN SR-338

Acknowledgements

References

1. Fitch, J.P., Lehman, S.K., Dowla, F.W., Lu, S.Y., Johansson, E.M., Goodman, D. M. Ship-wake detection procedure using conjugate gradient trained artificial neural networks. *IEEE Transactions on Geoscience and Remote Sensing*, **29**, 1991:718-726.

2. Rey, M., Tunaley, J.K.E., Sibbald, T. Use of the Dempster-Shafer algorithm for the detection of SAR ship wakes. *IEEE Transactions on Geoscience and Remote Sensing*, **31**, 1993:1141-1118.

3. Vachon, P.W., Campbell, J.W.M., Bjerkelund, C.A., Dobson, F.W., Rey, M.T. Ship detection by the RADARSAT SAR: validation of detection model predictions. *Canadian Journal of Remote Sensing*, **23**, 1997:48-59.

4. Eldhuset, K. An automatic ship and ship wake detection system for spaceborne SAR images in coastal regions. *IEEE Transactions on Geoscience and Remote Sensing*, **34**, 1996:1010-1018.

5. Askari, F., Zerr, B. A neural-network-fusion architecture for automatic extraction of oceanographic features from satellite remote sensing imagery. SACLANTCEN SR-306,

6. Shafer, G. A mathematical theory of evidence. Princeton University Press, Inc., Boston, 1989.

7. Stoffelen, A., Anderson, D.L.T. ERS-1 scatterometer data characteristics and wind retrieval skill. Proc. First ERS-1 Symposium, Noordwijk, The Netherlands, ESA SP-359, 1993.

8. Thompson, D.R., Beal, R.C. Mapping high-resolution wind fields using synthetic aperture radar. JHU/APL Technical Digest, **21**,2000:58-67, The Johns Hopkins University Applied Physics Laboratory, Laurel, MD.

9. Jakeman, E., Pusey, P.N. Statistics of non-Rayeigh microwave sea echo, *IEEE Transactions on Antennas and Propagation*, **24**, 1976:806-814.

10. Aksnes, K. SAR detection of ships and wakes, ESA Report, 2, Norwegian Defence Research Establishment, Kjeller, Norway, 1988.

11. Bezdek, J.C., Ehrlich, R. Full, W. The fuzzy c-means clustering algorithm. *Computers and Geosciences*, **10**, 1984:191-203.

12. Jain, A.K. Fundamentals of digital image processing. Prentice Hall, Englewood Cliffs, NJ, 1989.

13. Thompson, W. (Lord Kelvin), On the waves produced by a single impulse in water of any depth or in dispersive medium. *Proceedings of the Royal Society London*, Series A, **42**, 1887:80-85.

14. Munk, W.H., Scully-Power, R.S., Zachariasen, F. Ships from Space. *Proceedings of the Royal Society London*, A, **412**, 1987:231-254.

15. Griffin, O.M., Peltzer, R.D., Reed, A.M., Beck, R.F. Remote sensing of surface ship wakes. *Naval Engineers Journal*, **104**, 1992:245-258.

16. Lyden, J.D., Hammond, R.R., Lyzenga, D.R., Shuchman, R.A. Synthetic aperture radar imaging of surface ship wakes. *Journal of Geophysical Research*, **93**, 1986:12293-12300.

17. Hennings I, Romeiser, R., Alpers, W., Viola, A. Radar imaging of Kelvin arms of ship wakes. *International Journal of Remote Sensing*, **20**, 1999:2519-2543.

18. Ray, M.T., Tunaley, J.K.E., Folinsbee, J.T., Jahans, P.A., Dixon, J.A., Vant, M.R. Application of Radon transform techniques to wake detection in SEASAT-A SAR images. *IEEE Transactions on Geoscience and Remote Sensing*, **28**, 1990:553-560.

19. Wang, J., Howarth, P.J. Use of the Hough transform in automated lineament detection, *IEEE Transactions on Geoscience and Remote Sensing* **28**, 1990:561-566.

20. RADARSAT, data products and specifications, RSI-GS-026. RADARSAT International, Richmond, B.C., Canada, 1997.
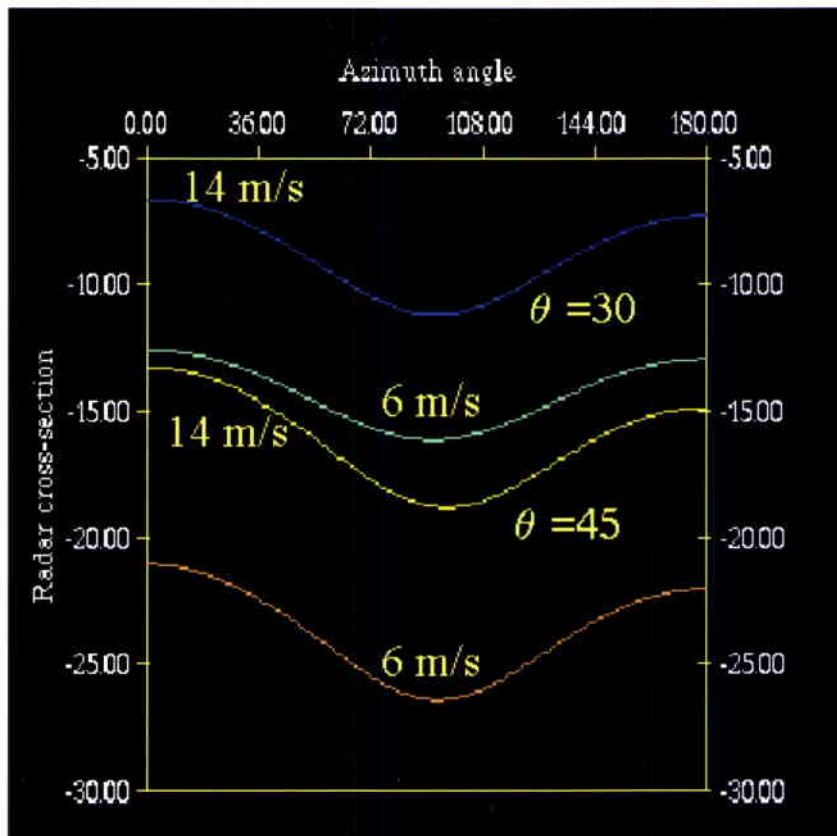
SACLANTCEN SR-338

Figure 1 *C-band (HH) radar cross-section vs azimuth angle for different incidence angles and wind speeds.*
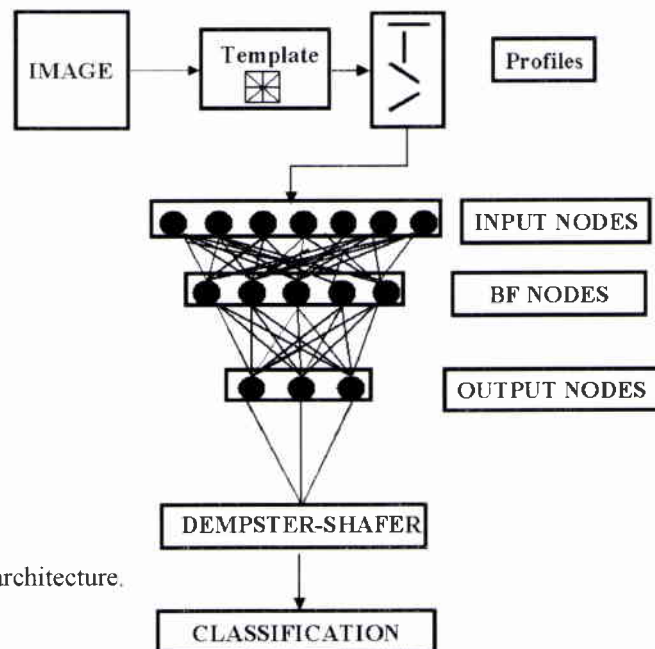

Figure 2 Neural network architecture.
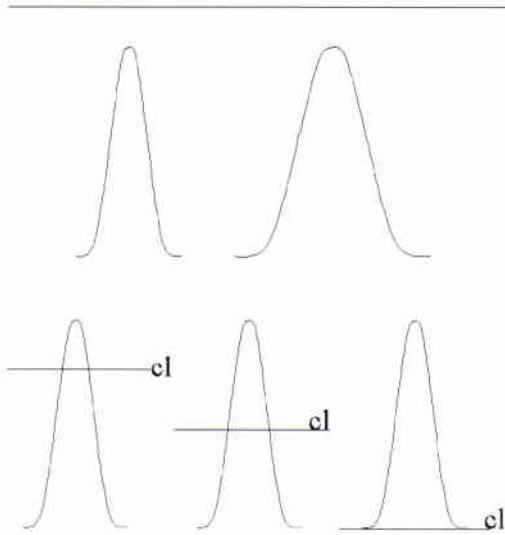
SACLANTCEN SR-338

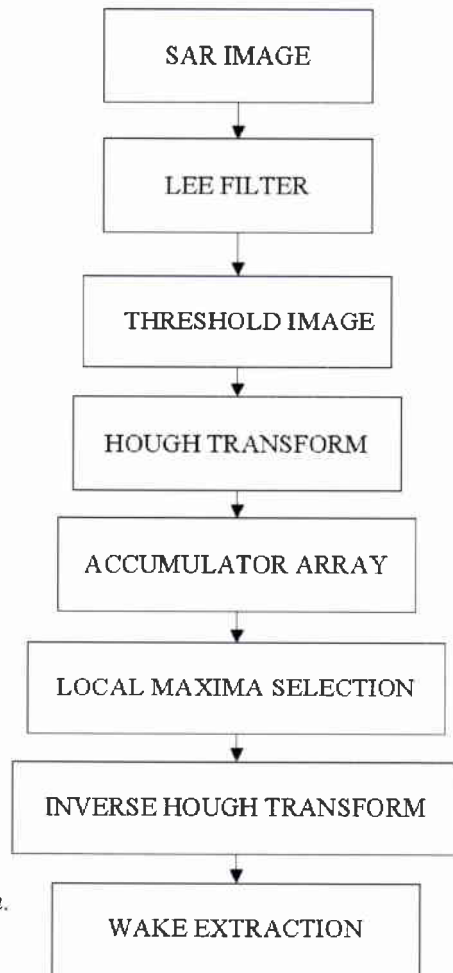**Figure 3** *Idealized shape used for training the network. C1 is the clutter level.*

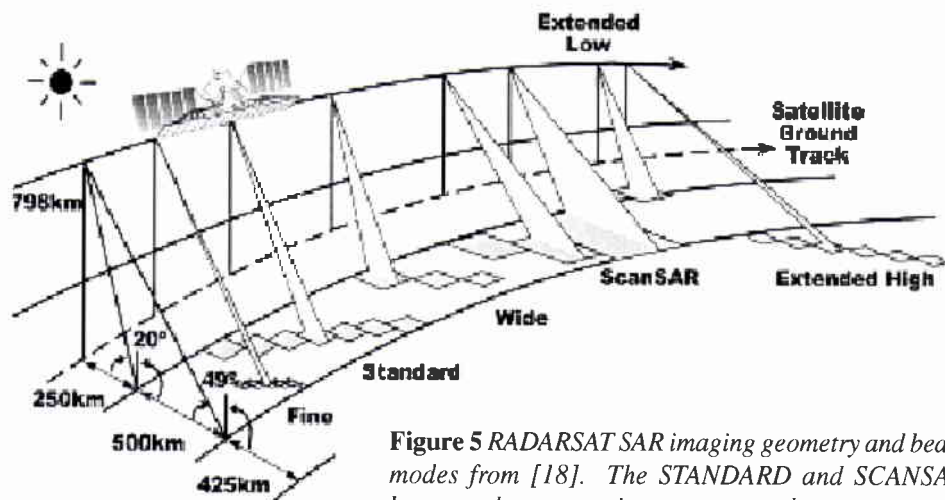**Figure 4** *Flowchart of procedure used in wake detection.*

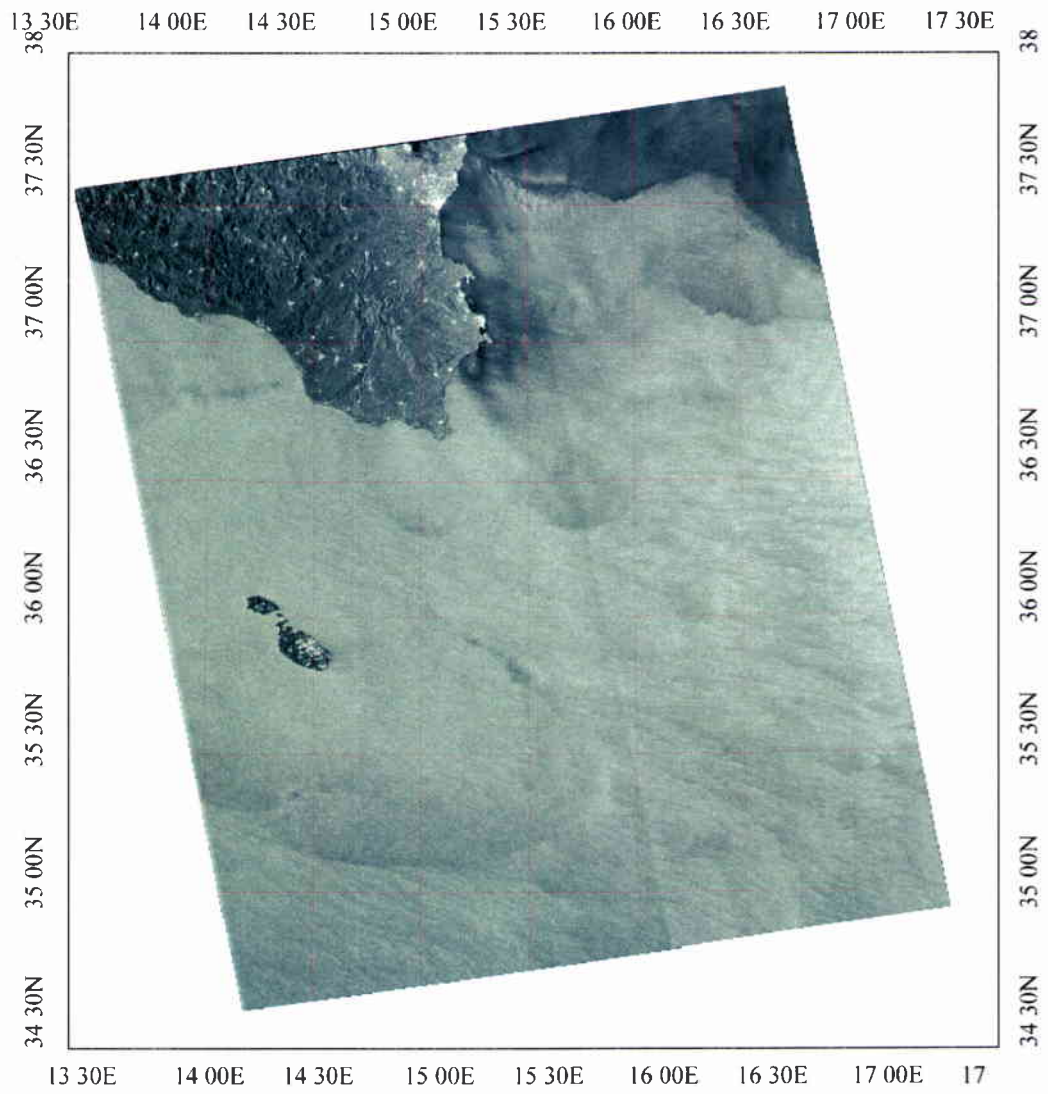**Figure 5** *RADARSAT SAR imaging geometry and beam modes from [18]. The STANDARD and SCANSAR beam modes are pertinent to our study.*

— 17 —

SACLANTCEN SR-338

**Figure 6** *RADARSAT SCANSAR image for March 2, 2000.*
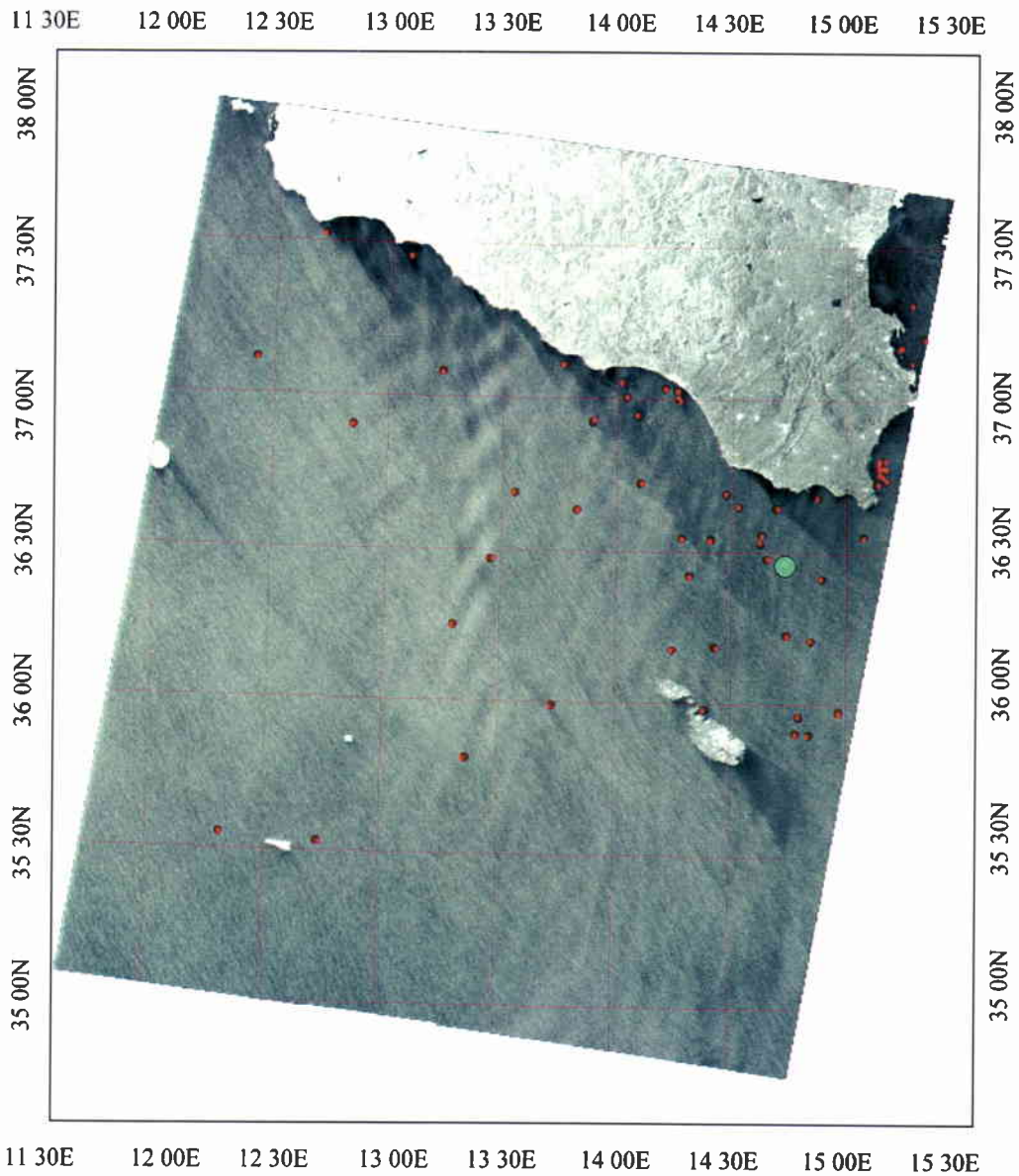
Figure 7 *RADARSAT SCANSAR image for March 3, 2000. The red dots represent ship locations based on visual detection. The blue dot identifies the location of R/V Alliance.*
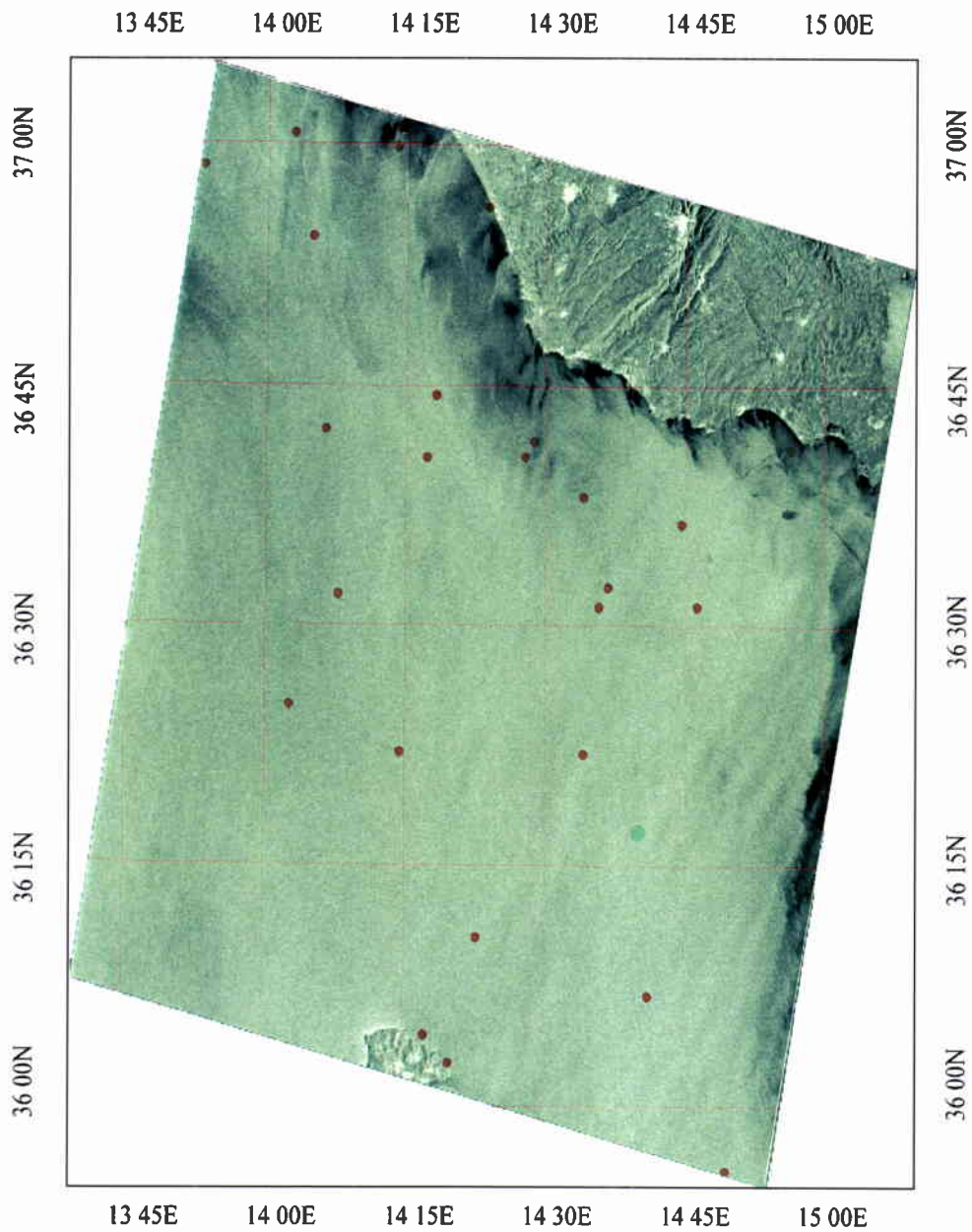
SACLANTCEN SR-338
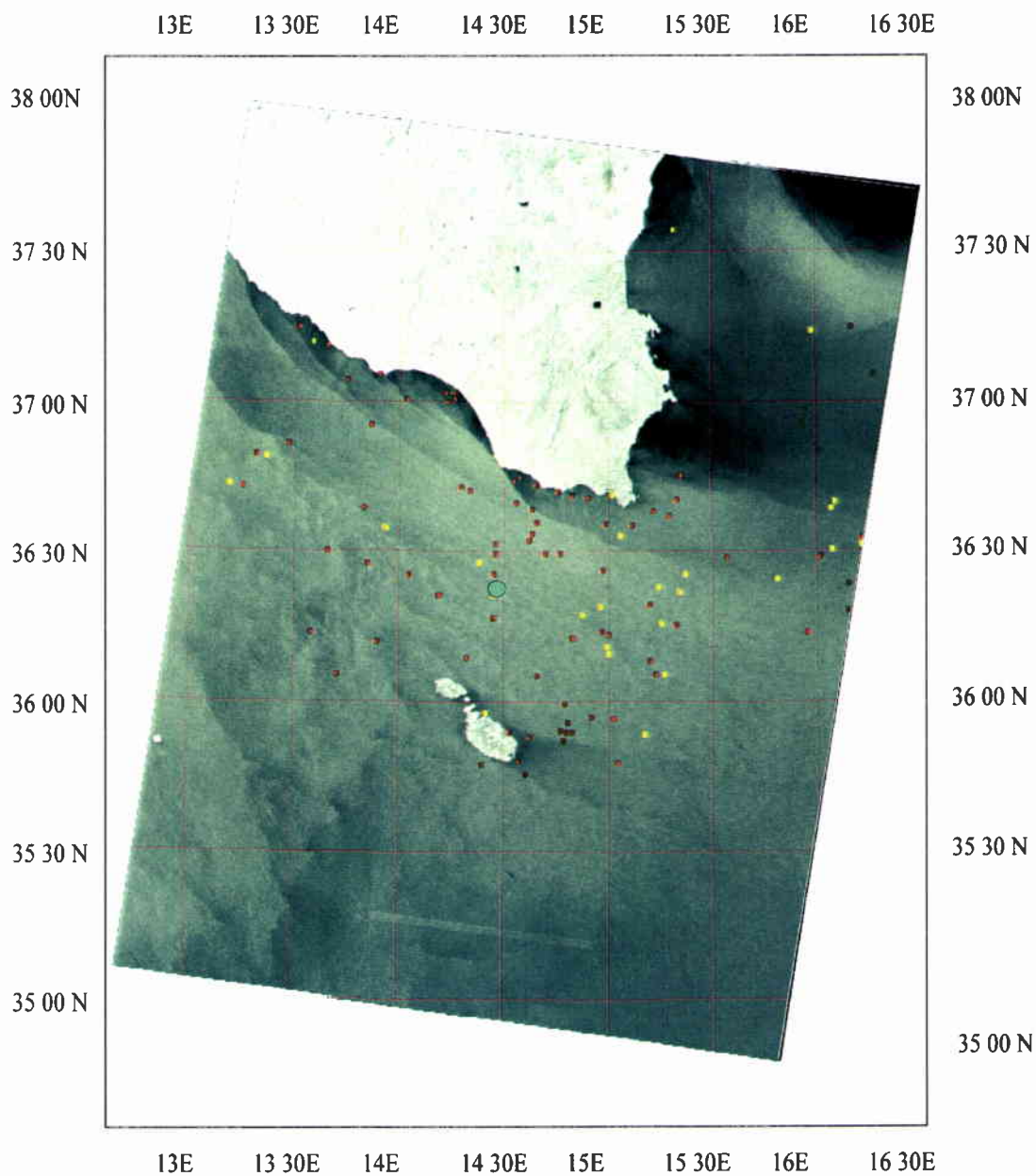
Figure 8 *RADARSAT SAR image for March 10, 2000. Red dots represent ship locations based on visual detection. The yellow dots represent ship locations based on MPA flight. The blue dot identifies the location of R/V Alliance.*
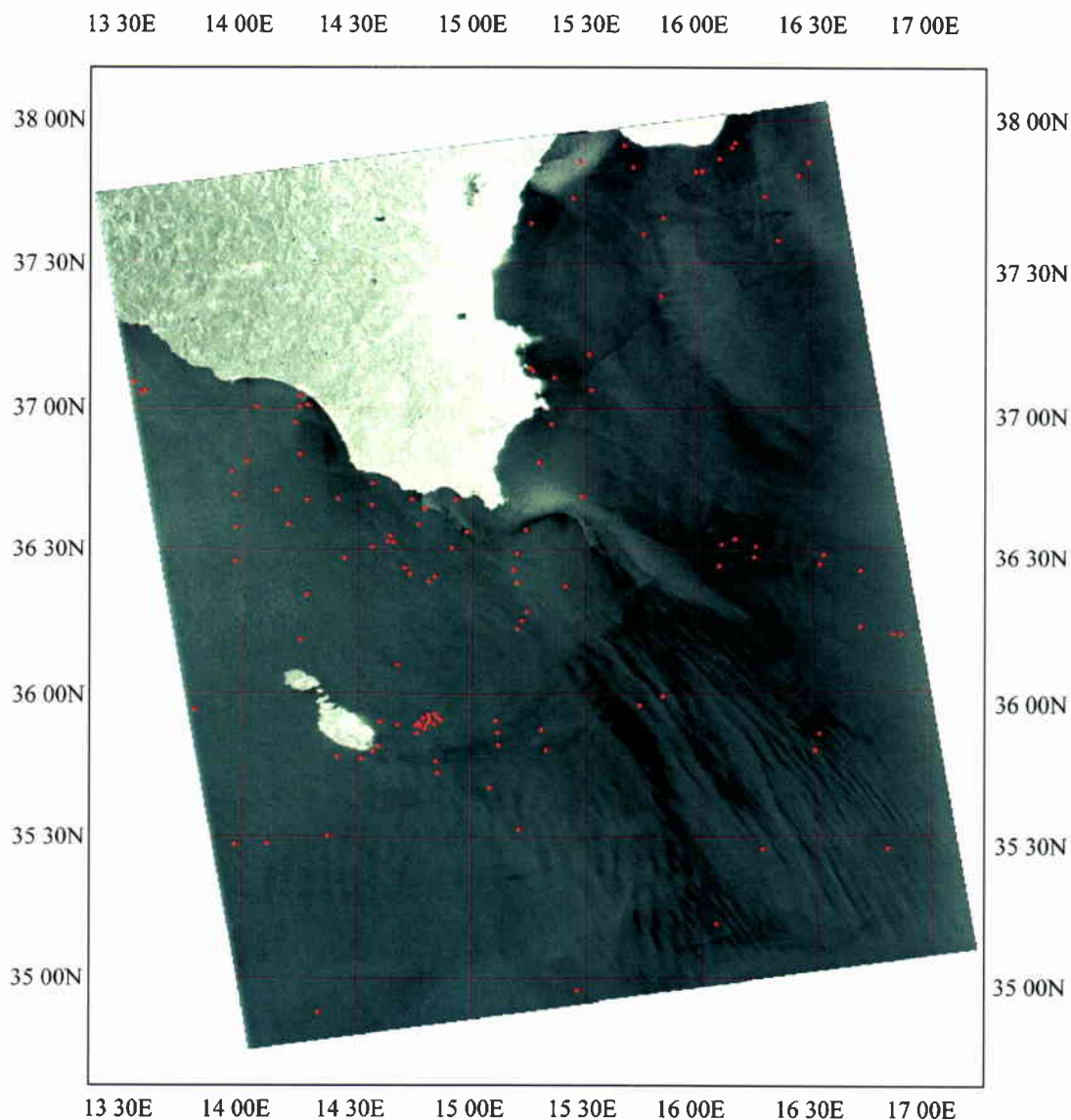
Figure 9 *RADARSAT SCANSAR image for March 12, 2000. The red dots represent ship locations based on visual detection.*

SACLANTCEN SR-338
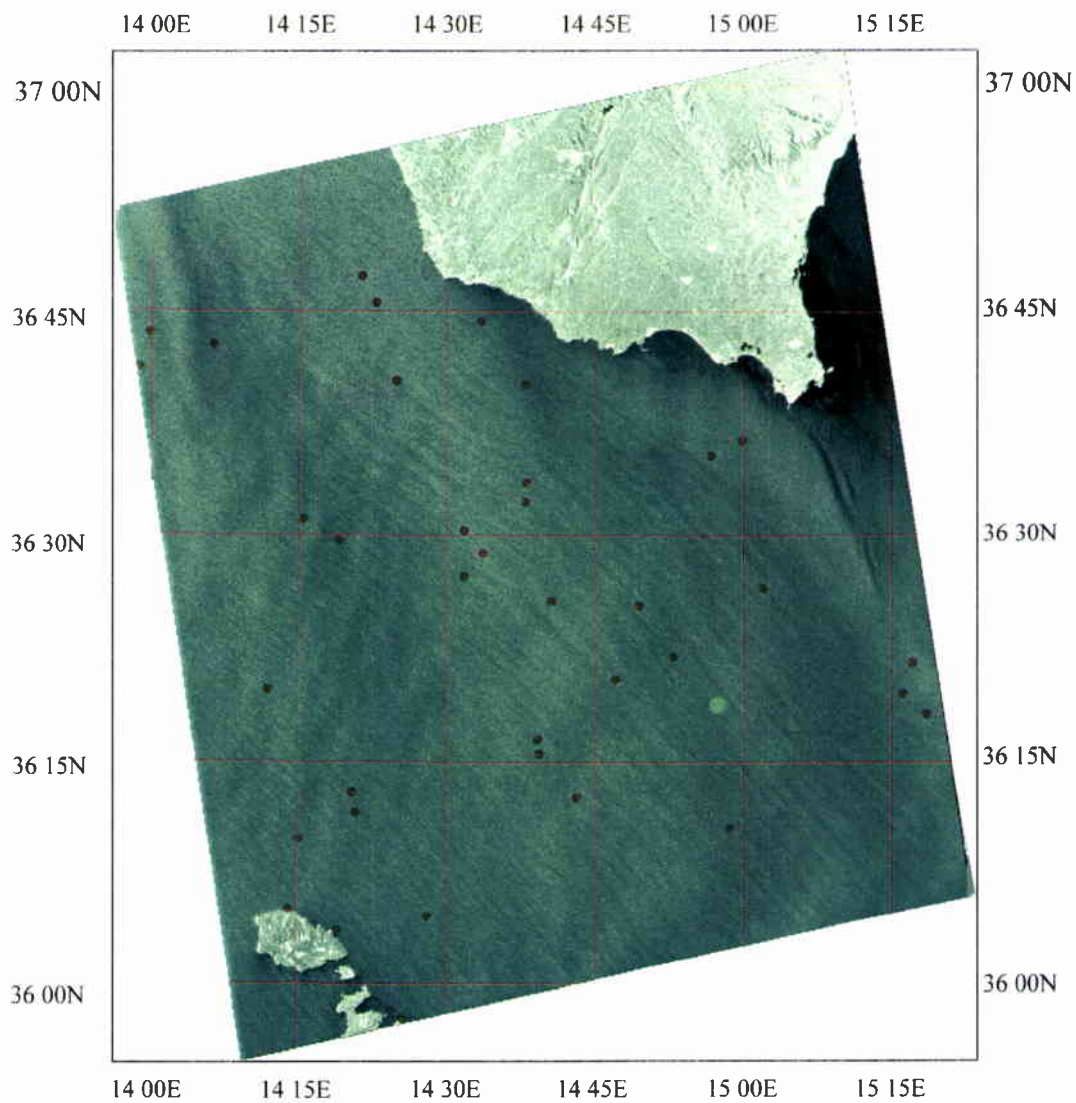
Figure 10 *RADARSAT STANDARD imagery for April 29, 2000. Red dots represent ship locations based on automatic detection. The blue dot identifies the location of R/V Alliance.*

Figure 11 *RADARSAT STANDARD SAR image for April 30, 2000. Red dots represent ship locations based on automatic detection. The blue dot identifies the location of R/V Alliance.*
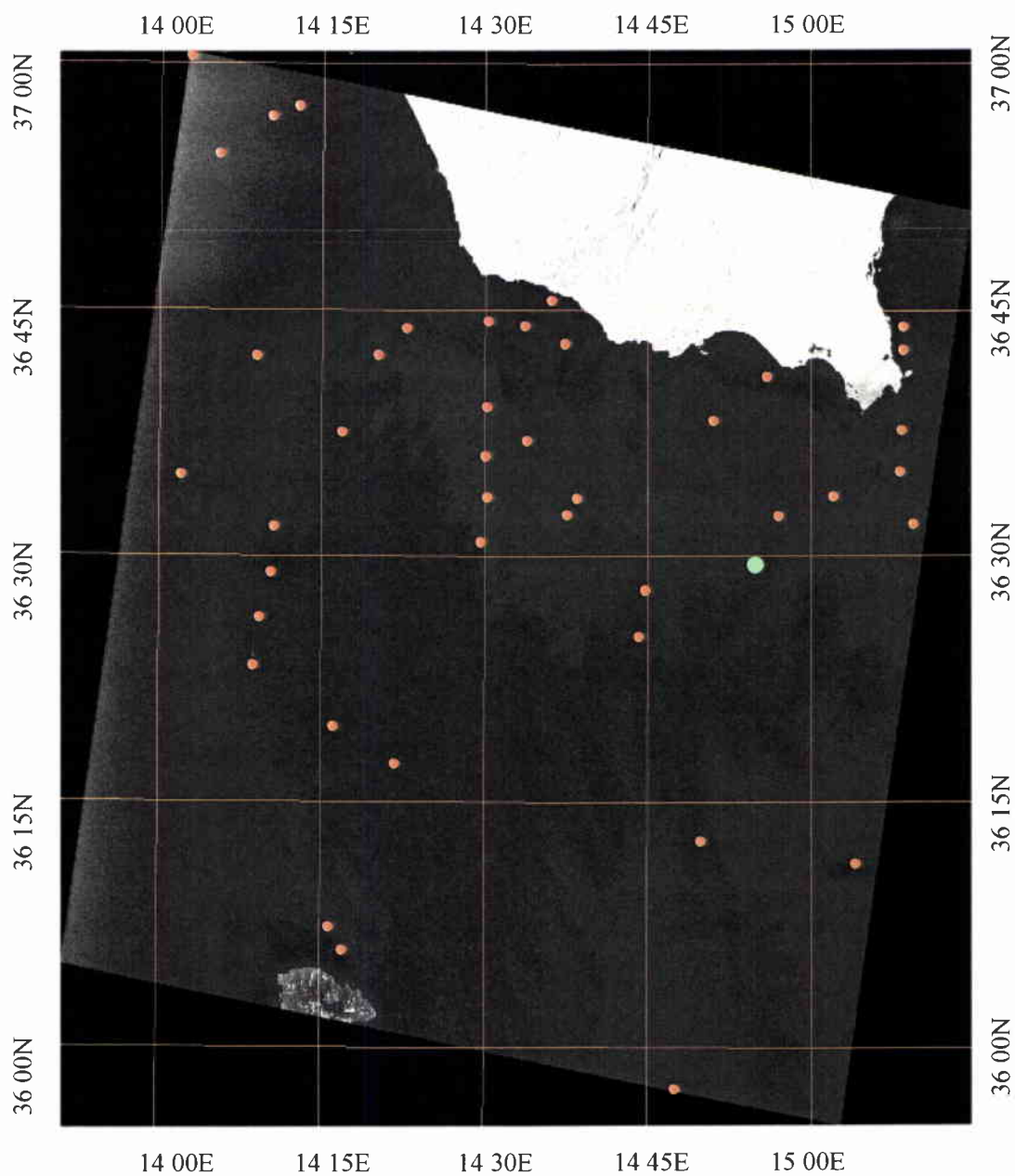
SACLANTCEN SR-338

Figure 12 *RADARSAT STANDARD imagery for May 04, 2000. Red dots represent ship locations based on automatic detection. The blue dot identifies the location of R/V Alliance.*
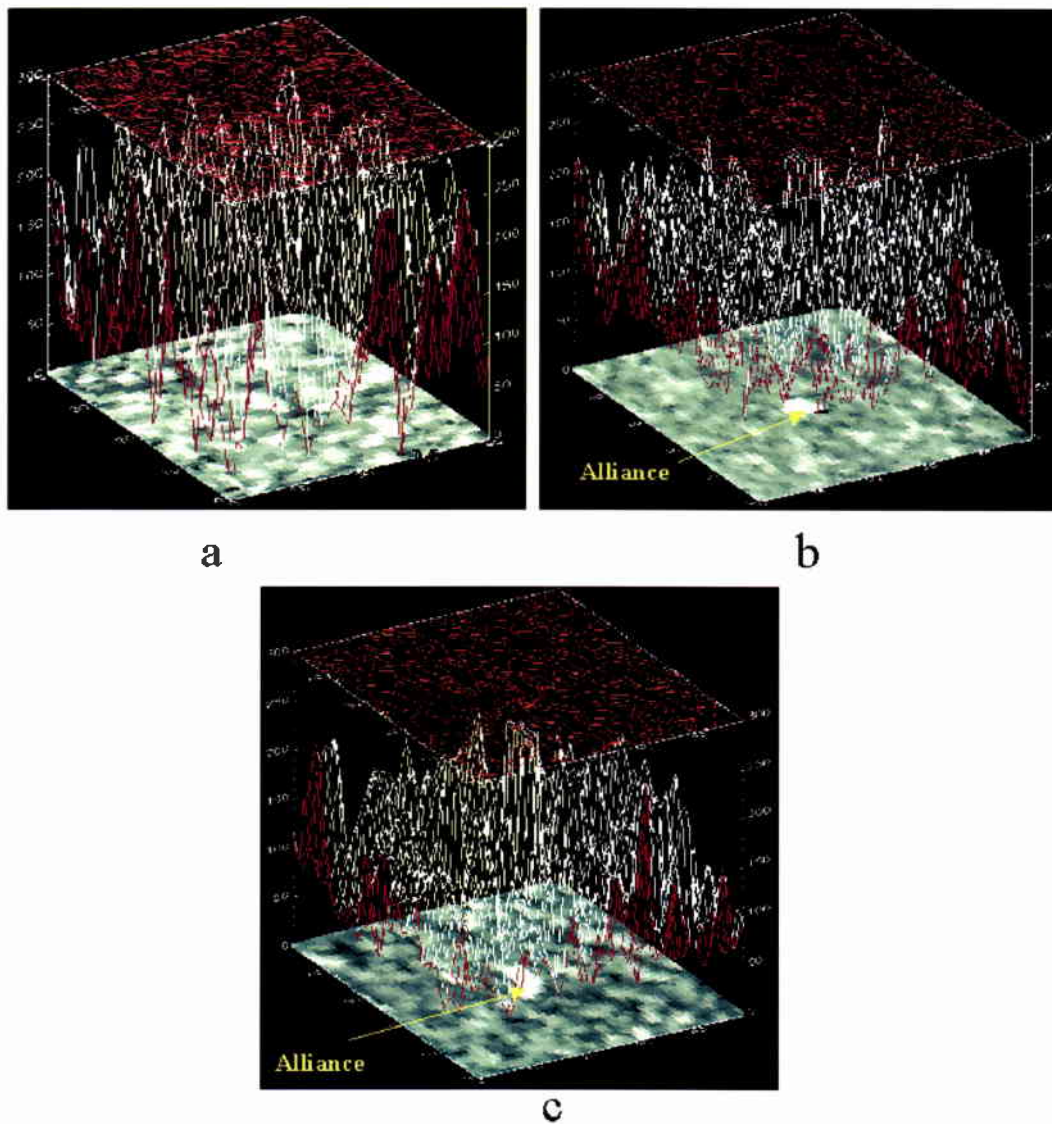
Figure 13 (a) *3-D plot of image intensity for region containing R/V Alliance for March 2, the signal from Alliance is not discernible from the background clutter; (b) same as (a) except for March 3, the Alliance signal-to-clutter ratio is 4.0 dB, the hard target return is 246 m wide; (c) same as (a) except for March 10, the Alliance signal-to-clutter ratio is 2.6 dB, the hard target return is 127 m wide.*
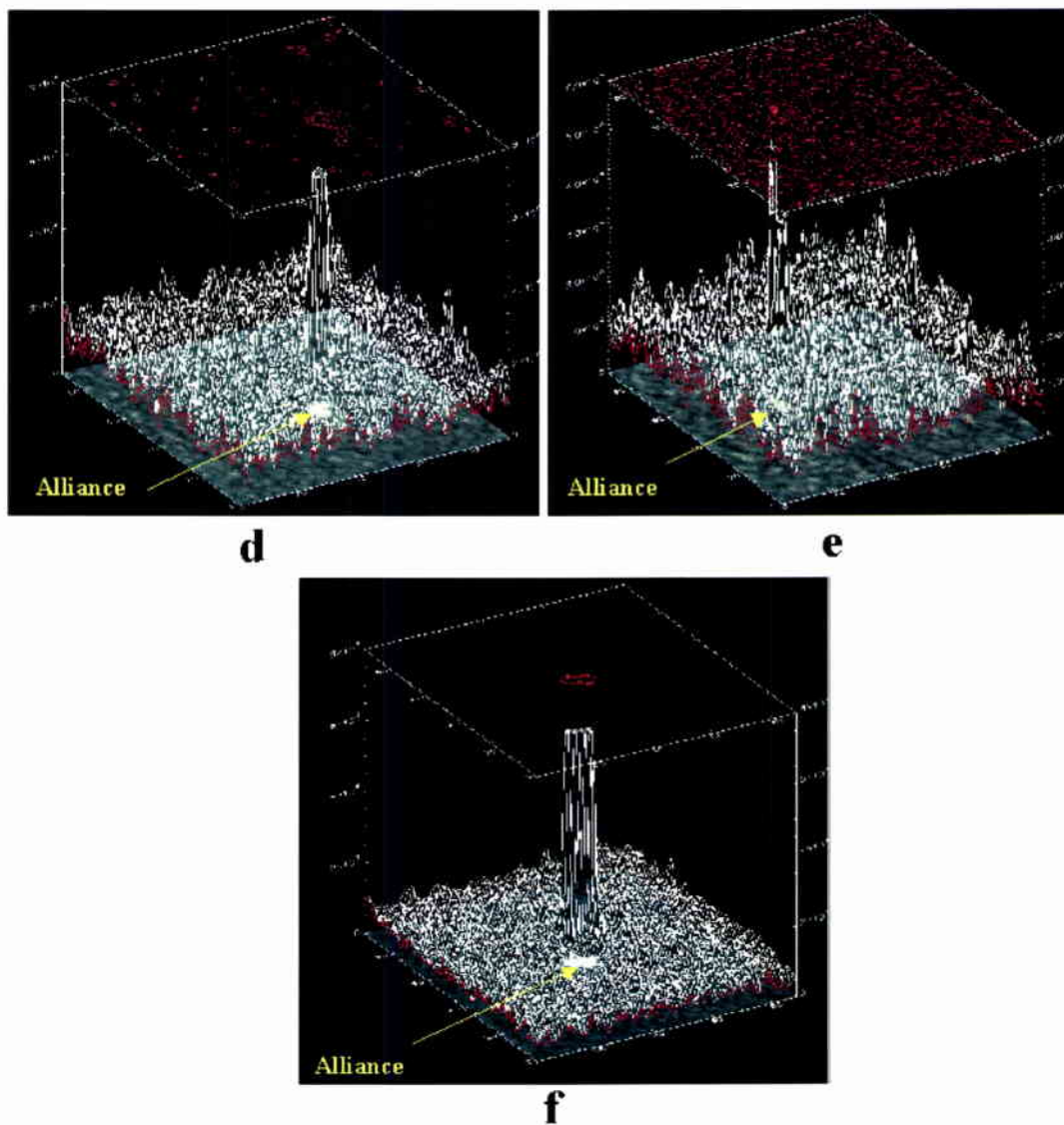
SACLANTCEN SR-338

Figure 13 (d) *same as (a) except for April 29, the Alliance signal-to-clutter ratio is 8.8 dB, the hard target return is 125 m wide; e) same as (a) except for April 30, the Alliance signal-to-clutter ratio is 7.0 dB, the hard target return is 137 m wide; (f) same as (a) except for May 4 the Alliance signal-to-clutter ratio is 10.8 dB, the hard target return is 125 m wide.*
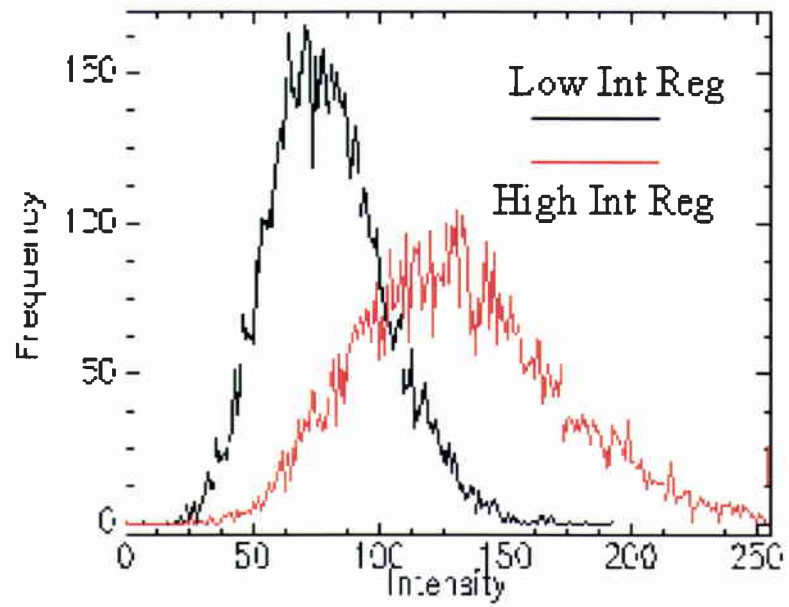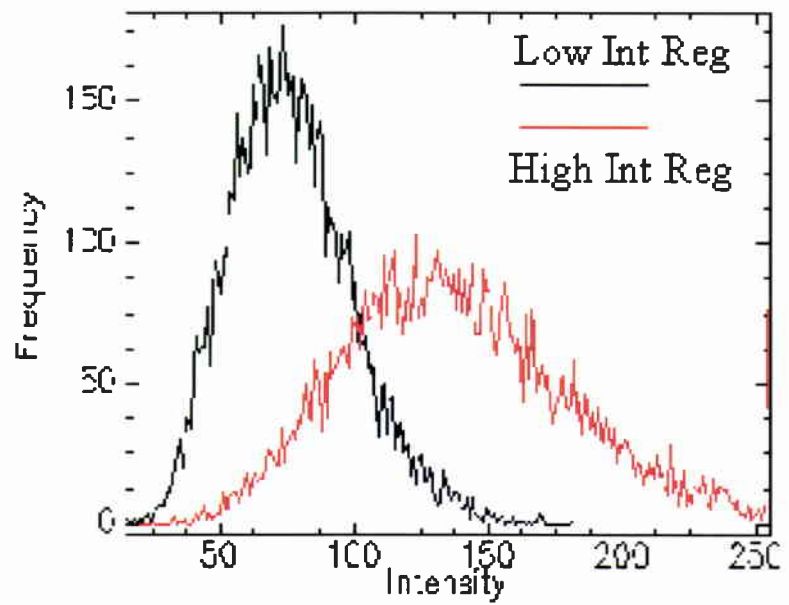
Figure 14 (a) *Histograms for sub-regions in March 03 scene containing low and high intensity values, (b) same as (a) except for March 10 scene.*
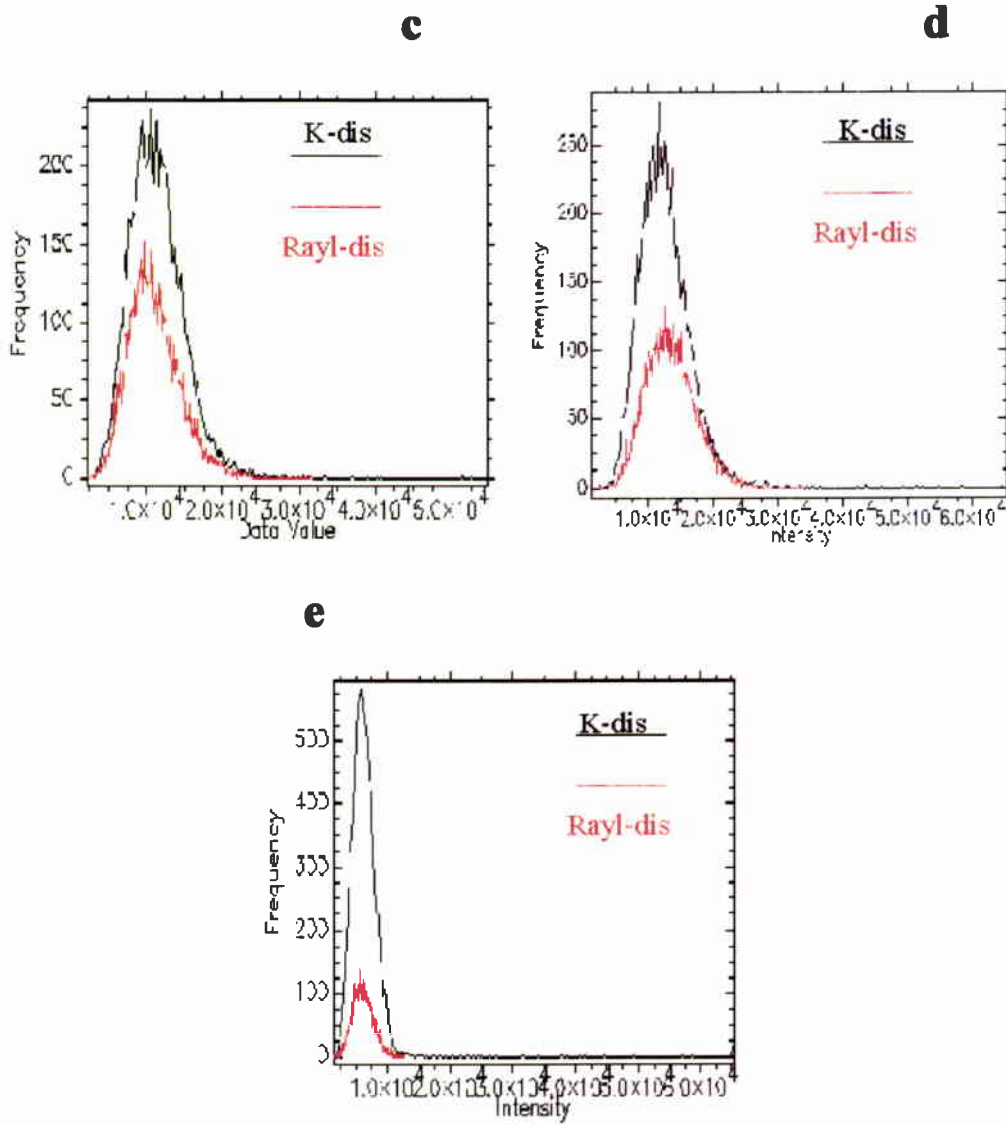
SACLANTCEN SR-338

Figure 14 (c) *Histograms for sub-regions in April 29 scene containing low and high intensity values, (d) same as (c) except for April 30 scene, (e) same as (c) except for May 04 scene, this subregion contains hard target.*
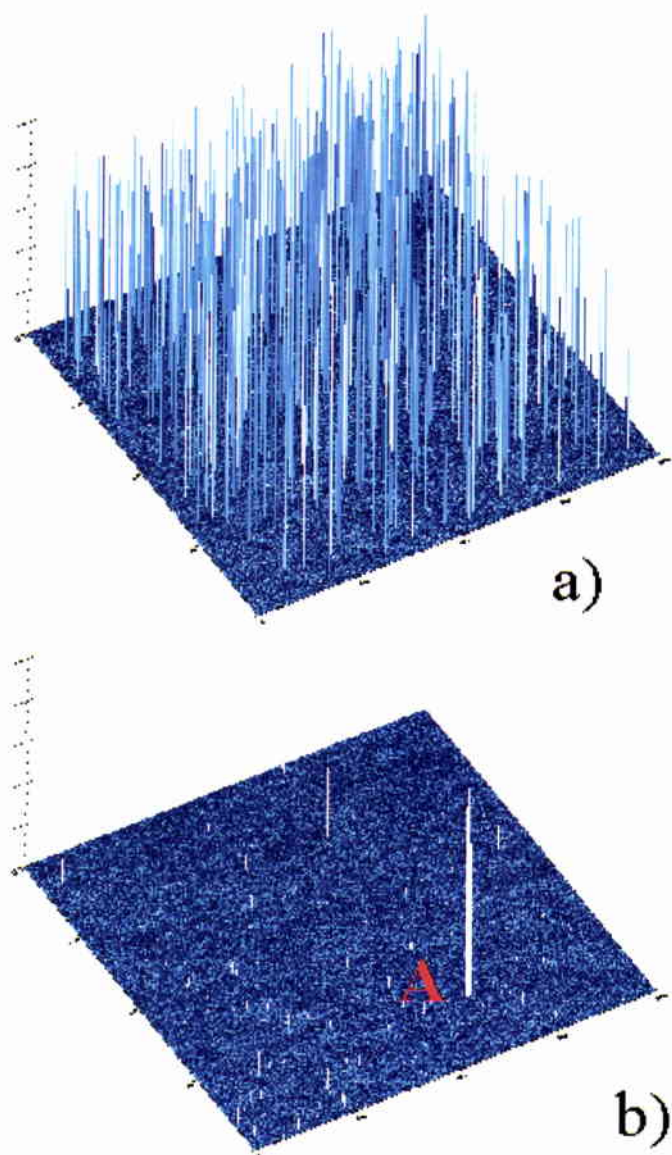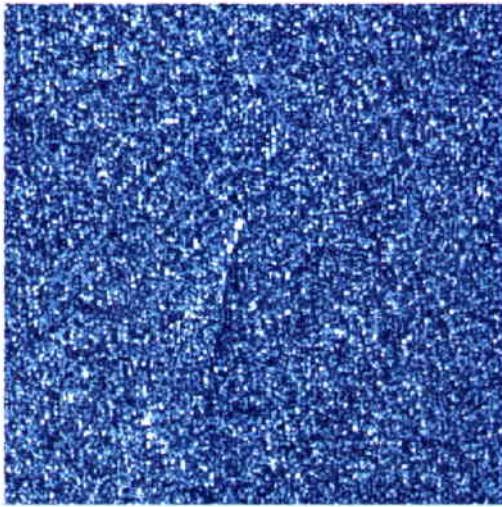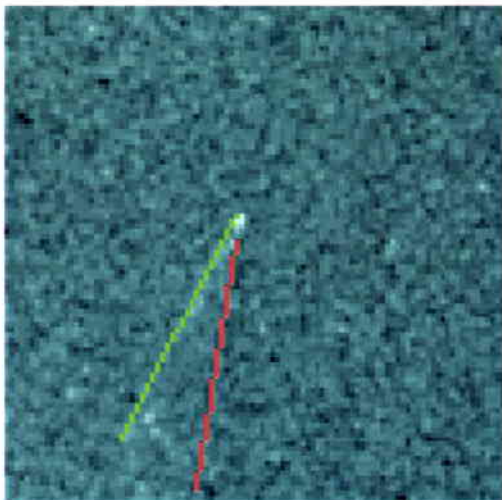
Figure 15 (a) *Application of NNDS to SCANSAR imagery; (b) Application of MM algorithm to same region. The red-A corresponds to the detected signal from the R/V Alliance.*

SACLANTCEN SR-338

Figure 16 (a) *Original SAR image; (b) Application of HT to the image showing the R/V Alliance wake.*

Table 1 *Minimum detectable ship length (m) based on HH scattering model.*

WIND M/S	INC ANG DEG	SHIP LEN CROSSWIND	SHIP LEN UPWIND
6	30	27	37
14	30	38	58
6	45	9	14
14	45	15	27

Table 2 *RADARSAT imaging parameters and environmental conditions.*

DATE	TIME (UT)	ORBIT TYPE	BEAM MODE	SWATH WIDTH (km)	RESOLUTION (m)	PIXEL SPACING (m)	INCIDENCE ANGLE	WINDS (m/s)	WAVES (m)
2-Mar	16:51:31	Ascending	SNA:W1+W2	300	50x50	25x25	20-39	11	4
3-Mar	5:06:17	Descending	SNB:W2+S5+S6	300	50x50	25x25	31-46	14	4.5
10-Mar	5:02:08	Descending	SNB:W2+S5+S6	300	50x50	25x25	31-46	7	1.2
12-Mar	16:59:57	Ascending	SNB:W2+S5+S6	300	50x50	25x25	31-46	5.5	0.9
29-Apr	16:59:24	Ascending	S4	100	24x27	12.5x12.5	20-27	10.3	2
30-Apr	5:14:52	Descending	S1	100	23x27	12.5x12.5	34-40	6	1.3
4-May	4:58:18	Descending	S6	100	20x27	12.5x12.5	41-46	3	1

Table 3 *Comparison of ship positions with SAR-derived positions.*

DATE	TIME UT	SPEED KTS	HEADING DEG	LATITUDE SHP-INS	LONGITUDE SHP-INS	OFFSET M	LATITUDE SAR-IMG	LONGITUDE SAR-IMG
2-Mar	16.51	21	290	36.504	14.584	-	-	-
3-Mar	5.06	26	292	36.466	14.726	179	36.466	14.724
10-Mar	5.02	6	116	36.424	14.457	421	36.422	14.453
12-Mar	16.59	-	in	in	port	-	port	-
29-Apr	16.59	0.2	288	36.317	14.952	90	36.317	14.953
30-Apr	5.14	12.6	181	36.311	14.748	428	36.308	14.751
4-May	4.58	3.2	81	36.494	14.906	222	36.492	14.906

Document Data Sheet

Security Classification		Project No. 01-B

Document Serial No. SR-338	Date of Issue December 2000	Total Pages 36 pp.

Author(s)

Askari, F., Zerr, B.

Title

An Automatic Approach to Ship Detection in Spaceborne Synthetic Aperture Radar Imagery: An Assessment of RADARSAT ship detection capability

Abstract

This report describes a methodology for automated ship and wake detection in space-based synthetic aperture radar (SAR) imagery. The methodology incorporates a multistage approach involving several algorithms which can be applied according to requirements, computational resources, and scene composition. We suggest that the localized K-distribution be used for scene segmentation and identification of regions containing probable targets. For a more detailed quantitative scene analysis and accountability for probabilities of occurrence of targets in conjunction with other oceanic features, a coupled neural-networks/Dempster-Shafer detection system is used. The mathematical morphology algorithm is better suited for SAR imagery with low signal-to-clutter ratios, as it incorporates neighbouring information and signal amplitudes for target detection. The methods are tested on several RADARSAT images with different imaging geometry and beam modes. On the basis of our findings, concerning the use of different RADARSAT imaging modes, we demonstrate conclusively that the STANDARD beam is far superior to SCANSAR-NARROW beam for automatic ship detection

Keywords

remote sensing, ship detection, K-distribution, artificial neural networks, RADARSAT, Hough transform

Issuing Organization

North Atlantic Treaty Organization
SACLANT Undersea Research Centre
Viale San Bartolomeo 400, 19138 La Spezia, Italy

[From N. America: SACLANTCEN
(New York) APO AE 09613]

Tel: +39 0187 527 361
Fax:+39 0187 527 700

E-mail: library@saclantc.nato.int

The SACLANT Undersea Research Centre provides the Supreme Allied Commander Atlantic (SACLANT) with scientific and technical assistance under the terms of its NATO charter, which entered into force on 1 February 1963. Without prejudice to this main task - and under the policy direction of SACLANT - the Centre also renders scientific and technical assistance to the individual NATO nations.

This document is approved for public release.
Distribution is unlimited

SACLANT Undersea Research Centre
Viale San Bartolomeo 400
19138 San Bartolomeo (SP), Italy

tel: +39 0187 527 (1) or extension
fax: +39 0187 527 700

e-mail: library@saclantc.nato.int

NORTH ATLANTIC TREATY ORGANIZATION